A&A 627, A60 (2019)
https://doi.org/10.1051/0004-6361/201935300

Astronomy & Astrophysics

Ground-based infrared mapping of H_2O_2 on Mars near opposition

T. Encrenaz[1], T. K. Greathouse[2], S. Aoki[3], F. Daerden[3], M. Giuranna[4], F. Forget[5], F. Lefèvre[6], F. Montmessin[6], T. Fouchet[1], B. Bézard[1], S. K. Atreya[7], C. DeWitt[8], M. J. Richter[9], L. Neary[3], and S. Viscardy[3]

[1] LESIA, Observatoire de Paris, CNRS, PSL University, Sorbonne Université, Sorbonne Paris Cité, 92195 Meudon, France
e-mail: therese.encrenaz@obspm.fr
[2] SwRI, Div. 15, San Antonio, TX 78228, USA
[3] Planetary Aeronomy Team, BIRA-IASB, 3 Avenue Circulaire, 1180 Brussels, Belgium
[4] IAPS–INAF, Via del Fosso del Cavaliere 100, 00133 Rome, Italy
[5] LMD, IPSL, 75252 Paris Cedex 05, France
[6] LATMOS, IPSL, 75252 Paris Cedex 05, France
[7] Climate and Space Sciences and Engineering Department, University of Michigan, Ann Arbor, MI 48109-2143, USA
[8] SOFIA Science Center, Ames Research Center, Moffett Field, Mountain View, CA 94035, USA
[9] Department of Physics, University of California Davis, CA 95616, USA

Received 18 February 2019 / Accepted 11 May 2019

ABSTRACT

We pursued our ground-based seasonal monitoring of hydrogen peroxide on Mars using thermal imaging spectroscopy, with two observations of the planet near opposition, in May 2016 (solar longitude Ls = 148.5°, diameter = 17 arcsec) and July 2018 (Ls = 209°, diameter = 23 arcsec). Data were recorded in the 1232–1242 cm^{-1} range (8.1 μm) with the Texas Echelon Cross Echelle Spectrograph (TEXES) mounted at the 3 m Infrared Telescope Facility (IRTF) at the Mauna Kea Observatories. As in the case of our previous analyses, maps of H_2O_2 were obtained using line depth ratios of weak transitions of H_2O_2 divided by a weak CO_2 line. The H_2O_2 map of April 2016 shows a strong dichotomy between the northern and southern hemispheres, with a mean volume mixing ratio of 45 ppbv on the north side and less than 10 ppbv on the south side; this dichotomy was expected by the photochemical models developed in the LMD Mars Global Climate Model (LMD-MGCM) and with the recently developed Global Environmental Multiscale (GEM) model. The second measurement (July 2018) was taken in the middle of the MY 34 global dust storm. H_2O_2 was not detected with a disk-integrated 2σ upper limit of 10 ppbv, while both the LMD-MGCM and the LEM models predicted a value above 20 ppbv (also observed by TEXES in 2003) in the absence of dust storm. This depletion is probably the result of the high dust content in the atmosphere at the time of our observations, which led to a decrease in the water vapor column density, as observed by the PFS during the global dust storm. GCM simulations using the GEM model show that the H_2O depletion leads to a drop in H_2O_2, due to the lack of HO_2 radicals. Our result brings a new constraint on the photochemistry of H_2O_2 in the presence of a high dust content. In parallel, we reprocessed the whole TEXES dataset of H_2O_2 measurements using the latest version of the GEISA database (GEISA 2015). We recently found that there is a significant difference in the H_2O_2 line strengths between the 2003 and 2015 versions of GEISA. Therefore, all H_2O_2 volume mixing ratios up to 2014 from TEXES measurements must be reduced by a factor of 1.75. As a consequence, in four cases (Ls around 80°, 100°, 150°, and 209°) the H_2O_2 abundances show contradictory values between different Martian years. At Ls = 209° the cause seems to be the increased dust content associated with the global dust storm. The inter-annual variability in the three other cases remains unexplained at this time.

Key words. planets and satellites: composition – planets and satellites: terrestrial planets – infrared: planetary systems – infrared: general

1. Introduction

Hydrogen peroxide H_2O_2 is known to be a key molecule in the photochemistry of the Martian atmosphere. At the time of the Viking exploration, this molecule was suggested as the potential oxidizer responsible for the absence of organics on the surface of Mars (Oyama & Berdahl 1977). The presence of H_2O_2 was expected, with volume mixing ratios (vmr) of a few parts per billion at most, on the basis of photochemical models (Krasnopolsky 1993, 2009; Clancy & Nair 1996; Atreya & Gu 1995). Hydrogen peroxide was first detected from the ground in the submillimeter range (Clancy et al. 2004), then it was repeatedly mapped with ground-based imaging spectroscopy in the thermal infrared range to study its seasonal cycle, using the Texas Echelon Cross Echelle Spectrograph (TEXES) mounted on the Infrared Telescope Facility (IRTF) at the Mauna Kea Observatories (Encrenaz et al. 2004, 2012, 2015). This dataset has been compared with photochemical models developed in the frame of the Mars Global Climate Model of the Laboratoire de Météorologie Dynamique (LMD-MGCM, Forget et al. 1999), and has been shown to favor heterogeneous chemistry with respect to gas-phase chemistry (Lefèvre et al. 2008).

We took advantage of two favorable oppositions of Mars, in May 2016 and July 2018, to obtain new maps of H_2O_2 at high spatial resolution. Then we were able to observe Mars in the middle of the M34 global dust storm, which gave us an unexpected opportunity to study the behavior of H_2O_2 in the presence of a large dust content. While the H_2O_2 map of May 2016 was in full agreement with the expectations, the H_2O_2 abundance in July 2018 was surprisingly low. The present paper reports these two new observations.

In the present analysis, we used the GEISA 2015 spectroscopic database. We found that there is a significant difference between the H_2O_2 line strengths reported in GEISA 2015 and those of GEISA 2003, used for our earlier analyses, with the 2015 values being higher by a factor close to 1.75. This problem is addressed in more detail in Sect. 4.1. As a result, we recalibrated the whole H_2O_2 dataset using the new GEISA values.

In Sect. 2 we describe the observation of May 2016 and its comparison with the global climate models. In Sect. 3 we present the results of the July 2018 observations. In Sect. 4 we first present the whole H_2O_2 dataset using the GEISA 2015 spectroscopic database. Then we analyze the discrepancy observed between the TEXES data of July 2018 and the models, and we propose an interpretation associated with the high dust content of the MY 34 global dust storm. Finally, we discuss the whole H_2O_2 dataset and we note several cases of inter-annual variations, which remain unexplained at this time. Our conclusions are summarized in Sect. 5.

2. Ls = 148.5° (May 2016)

2.1. TEXES observations

The Texas Echelon Cross Echelle Spectrograph (TEXES) is an imaging spectrometer operating between 5 and 25 μm that combines a high resolving power (above 80 000 at 8 μm in the high-resolution mode) and a good spatial resolution (about 1 arcsec). A full description of the instrument can be found in Lacy et al. (2002). We used the instrument at the 3 m Infrared Telescope Facility (IRTF) at the Mauna Kea Observatories (Hawaii). As we did in the case of our first observation in 2003 (Encrenaz et al. 2004, 2012), we used the 1230–1236 cm^{-1} spectral range (8.09–8.13 μm) where weak transitions of CO_2 and H_2O_2 are present.

Data were recorded on May 7, 2016, between 08:00 and 9:00 UT. The solar longitude (Ls) of Mars was 148.5°. The diameter of the planet was 17.0 arcsec and its illumination factor was 98.8%. We used a 1.1 × 8 arcsec slit, aligned along the celestial north-south axis, and we stepped the telescope by 0.5 arcsec in the west-east direction between two successive integrations in order to map the Martian disk. Because the slit length was much smaller than the diameter of Mars, we co-added three successive scans corresponding to the southern hemisphere, the central region, and the northern hemisphere of the planet. The total observing time was about 45 min. The mean longitude of the sub-Earth point during the observation was 75° W.

The disk-integrated spectrum is shown in Fig. 1. The Doppler shift at 1234 cm^{-1} is + 0.031 cm^{-1}. The TEXES data cubes are calibrated using the radiometric method commonly used for submillimeter/millimeter astronomy, which is described in detail in Lacy et al. (2002).

As in the case of our previous observations, we chose weak transitions of H_2O_2 and CO_2, well isolated from telluric lines. Using the GEISA 2015 database (which is in agreement with the HITRAN 2016 dabase), we selected the same parameters as were used for our first observation in June 2003: the H_2O_2 doublet of the ν_6 band at 1234.011 cm^{-1} ($I = 2.650 \times 10^{-20}$ cm molec^{-1}, $E = 267.926$ cm^{-1}) and 1234.055 cm^{-1} ($I = 2.82 \times 10^{-20}$ cm molec^{-1}, $E = 261.164$ cm^{-1}), which is close to a weak CO_2 isotopic (628) transition at 1233.929 cm^{-1} ($I = 4.13 \times 10^{-27}$ cm molec^{-1}, $E = 88.357$ cm^{-1}). Figure 1 shows the disk-integrated spectrum of Mars between 1232.5 and 1234.2 cm^{-1}, compared with the atmospheric transmission, as observed by the TEXES instrument, and a nominal synthetic spectrum calculated for a H_2O_2 volume mixing ratio of 100 ppbv, indicating the positions of the CO_2 and H_2O_2 transitions.

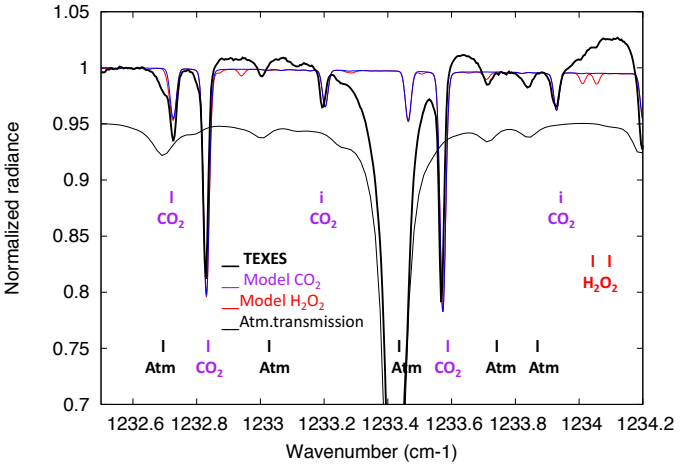

Fig. 1. Thick black line: spectrum of Mars between 1232.6 and 1234.2 cm^{-1}, integrated over the Martian disk, recorded on May 7, 2016 (Ls = 148.5°, normalized radiance). Synthetic spectra of Mars: CO_2 alone (blue), H_2O_2 alone with $H_2O_2/CO_2 = 100$ ppbv (red). Thin black line (in absolute units shifted by −0.05): transmission from the terrestrial atmosphere, as measured by the TEXES instrument. "Atm" indicates terrestrial absorption.

The H_2O_2 mixing ratio was estimated from the mean ratio of the line depths of the H_2O_2 doublet divided by the CO_2 line depth. As discussed in earlier papers (in particular, see Encrenaz et al. 2015), this first-order method minimizes the uncertainties associated with the surface and atmospheric parameters, as well as the effect of the airmass factor. We checked the linearity of the H_2O_2/CO_2 line depth ratio with respect to the H_2O_2 volume mixing ratio for a wide range of thermal profiles and for air masses as high as 5.0. This study has shown that the maximum departure is 10% for an airmass of 5.0 (Encrenaz et al. 2015). As in our previous studies, our mixing ratios, expressed by volume, are derived relative to carbon dioxide.

In the case of CO_2, we checked the consistency of our results by mapping several CO_2 lines whose intensities are comparable to that of the 1233.928 cm^{-1} transition. This comparison has shown that the 1233.929 cm^{-1} CO_2 transition is polluted by an instrumental artifact, with a spike appearing occasionally very close to the line center. We checked that this artifact was not present in our previous observation in June 2003; however, it also appeared on July 6, 2018, as we discuss below. For this reason, we used another CO_2 transition of comparable intensity at 1233.203 cm^{-1} ($I = 4.16 \times 10^{-27}$ cm molec^{-1}, $E = 100.137$ cm^{-1}) as a proxy of this line.

Figure 2 shows the maps of the continuum radiance (measured at 1233.95 cm^{-1}), the CO_2 line depth (measured for the 1233.203 cm^{-1} transition), and the mean value of the depths of the H_2O_2 lines at 1234.011 and 1234.055 cm^{-1}. For comparison, Fig. 3 shows the maps of the surface temperature and the temperature contrast $T(z = 1\text{km}) - Ts$ for the same season and the same geometry, derived from the LMD Mars Climate Database (MCD, Forget et al. 1999). The continuum radiance is at its maximum at the center of the scene, as expected since the sub-Earth point is in the early afternoon, close to the subsolar point; the strong decrease observed in the TEXES map toward the edge is primarily due to the increasing airmass of the colder atmosphere. The CO_2 line depth map measured by TEXES is the combination of three factors: (1) the surface pressure (hence the topography),

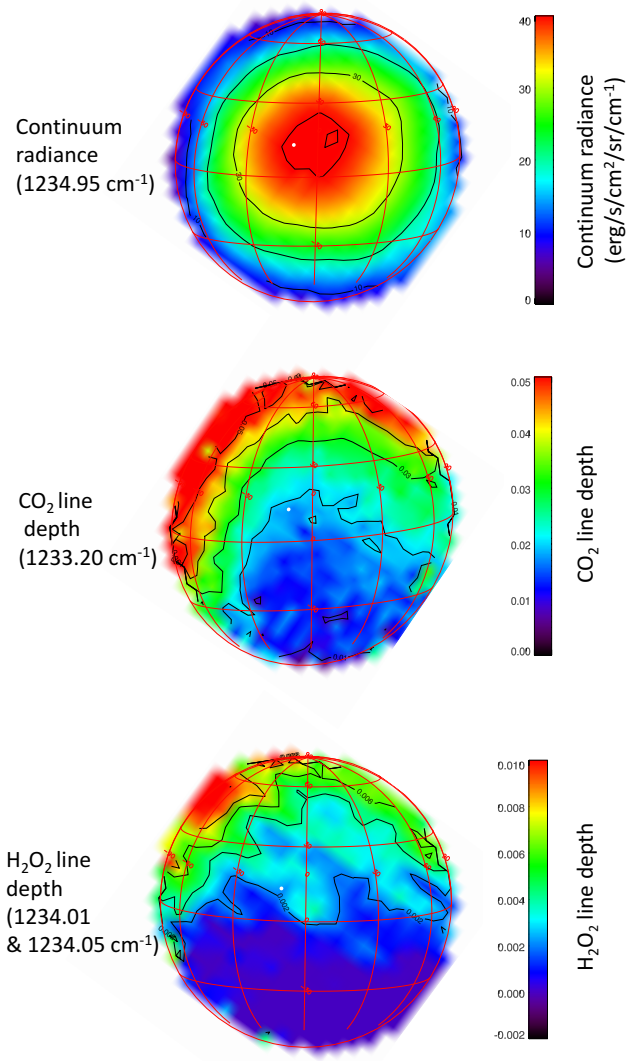

Fig. 2. Maps of the continuum radiance at 1233.95 cm^{-1} (*top*), the CO_2 line depth at 1233.203 cm^{-1} (*middle*), and the mean value of the H_2O_2 line depths at 1234.011 and 1234.055 cm^{-1} (*bottom*), recorded on May 7, 2016 (Ls = 148.5°). The Martian north pole is at the top of the figure. The subsolar point is shown (white dot).

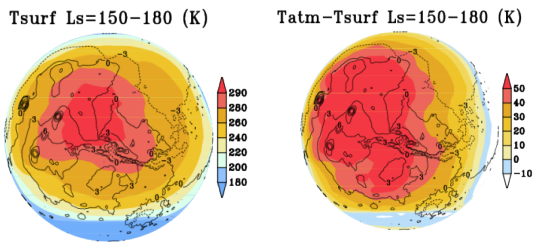

Fig. 3. Synthetic maps of (*left*) the surface temperature, and (*right*) the temperature contrast T(z=1km) – Ts, for the seasonal range Ls = 150–180°. The maps are from the Mars Climate Database (Forget et al. 1999).

(2) the temperature contrast between the atmosphere and the surface, and (3) the airmass. The airmass effect explains why the observed CO_2 line depth is highest on the northern and western limbs of the planet. The observed CO_2 line depth is low in the southeast part of the map because of the lower temperature contrast and the higher elevation. The H_2O_2 line depth is also affected by the same effects.

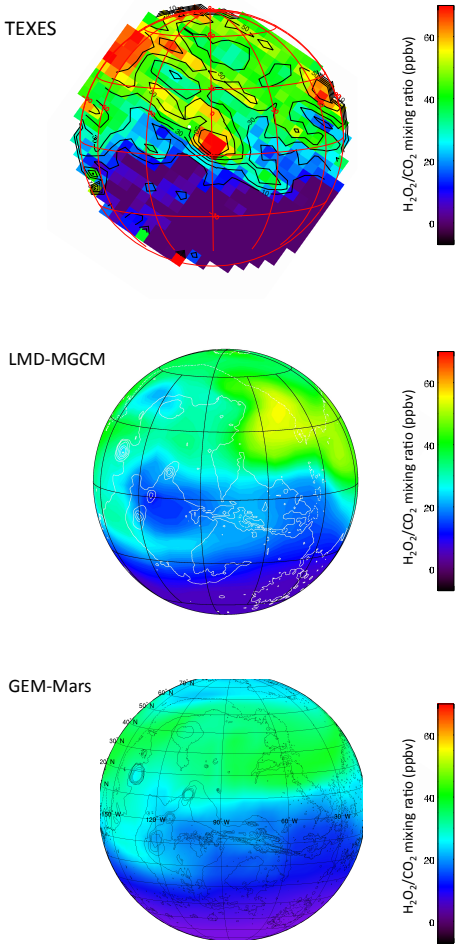

Fig. 4. *Top*: map of the H_2O_2/CO_2 volume mixing inferred from the H_2O_2/CO_2 line depth ratio, using the transitions shown in Fig. 2. The conversion factor between the H_2O_2 vmr and the H_2O_2 ldr is the following: vmr = 45.0/0.13 ldr (see text, Sect. 2.2). The subsolar point is shown as a white dot. *Middle*: synthetic map of the H_2O_2 vmr for Ls = 145–150° as predicted by the LMD-MGCM (Forget et al. 1999). *Bottom*: same synthetic map, generated by the GEM model (Daerden et al. 2019). The bright spots observed on the TEXES map at the limb may be an artifact, or due to the low signal near the limb, implying a larger error bar.

Figure 4 shows a map of the H_2O_2/CO_2 line depth ratio (ldr), using the transitions shown in Fig. 2, compared with two maps of the H_2O_2 volume mixing ratio, as predicted by the LMD-MGCM and the Global Environmental Multiscale (GEM) models. The three maps show a very good qualitative agreement, and all show a clear dichotomy between the northern and southern hemispheres.

2.2. Data interpretation and modeling

On the basis of the north-south dichotomy shown by our map (Fig. 3), we integrated the spectra separately in the northern and southern hemispheres, and we compared the integrated spectra in these two regions with synthetic models. The west longitude range was 75° ± 80° in both cases. The latitude range was (8° N–90° N) in the northern hemisphere and (50° S–8° N) in the southern hemisphere. We used the atmospheric parameters (surface pressure, surface temperature, and thermal profile) inferred from the MCD (Forget et al. 1999). For the northern and southern hemispheres the mean temperatures were 275 and 255 K at the surface, 225 and 218 K at $z = 1$ km, 197 and 192 K at $z = 10$ km,

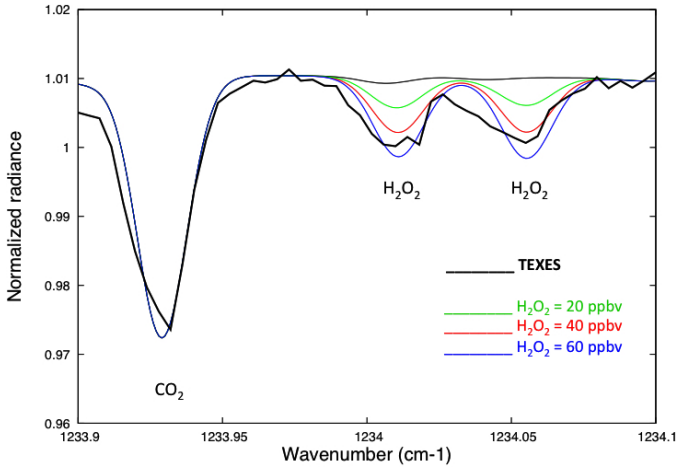

Fig. 5. Bold dark line: spectrum of Mars between 1233.9 and 1234.1 cm^{-1}, integrated over the northern hemisphere of the planet, recorded on May 7, 2016 (Ls = 148.5Å, normalized radiance). Thin lines: synthetic models, calculated using the atmospheric parameters described in Sect. 2.2: Black: H_2O_2 = 0 ppbv; green: H_2O_2 = 20 ppbv; red: H_2O_2 = 40 ppbv; blue: H_2O_2 = 60 ppbv. The best fit is obtained for a value of 45 ppbv. The spectral resolution of the models is 0.024 cm^{-1}.

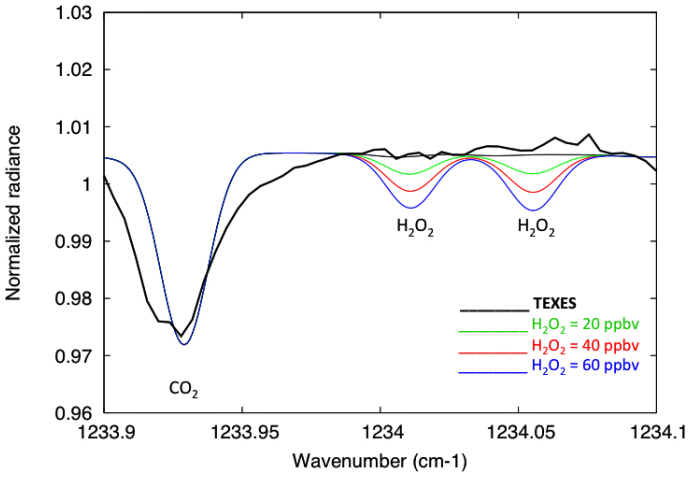

Fig. 6. Bold dark line: spectrum of Mars between 1233.9 and 1234.1 cm^{-1}, integrated over the southern hemisphere of the planet, recorded on May 7, 2016 (Ls = 148Å, normalized radiance). Thin lines: synthetic models, calculated using the atmospheric parameters described in Sect. 2.2: Black: H_2O_2 = 0 ppbv; green: H_2O_2 = 20 ppbv; red: H_2O_2 = 40 ppbv; blue: H_2O_2 = 60 ppbv. H_2O_2 is undetected, with a 2σ upper limit of 10 ppbv. The poor fit of the CO_2 line in the southern hemisphere is due to the occasional presence of a spike near the line center. The spectral resolution of the models is 0.024 cm^{-1}.

respectively, and 155 K for both hemispheres above z = 50 km. The mean surface pressure was 5.5 and 3.6 mbar for the northern and southern hemispheres, respectively. We then used the CO_2 transitions to check the consistency of these parameters, and we used them to model the H_2O_2 transitions. Calculations show that for all transitions the lines are mostly formed in the lower troposphere, within the first ten kilometers above the surface. From the synthetic spectra we derived the following relationship between the H_2O_2 volume mixing ratio and the H_2O_2/CO_2 line depth ratio corresponding to the transitions shown in Fig. 2:

$$H_2O_2\text{vmr(ppbv)} = 45.0/0.13 \times (H_2O_2/CO_2)\text{ldr}.$$

Our synthetic spectra were modeled using spectroscopic data extracted from the GEISA 2015 molecular database (Jacquinet-Husson et al. 2016). In the case of the CO_2 broadening coefficient, we used the values quoted by Pollack et al. (1993) and references therein. As in our previous analyses, we assumed for H_2O_2 a constant mixing ratio as a function of altitude. This assumption is actually required to infer the H_2O_2 volume mixing ratio from the H_2O_2/CO_2 line depth ratio. According to photochemical models, the H_2O_2 cutoff is expected to occur above an altitude of about 10 km near aphelion (northern spring and summer) and about 30 km around perihelion (southern spring and summer), and the H_2O_2 mixing ratio is more or less constant below this threshold (Encrenaz et al. 2012). Because the H_2O_2 and CO_2 lines are weak, they are formed in the first kilometers above the surface. We thus expect the assumption of a constant H_2O_2 mixing ratio to have a minor influence on our results. Figures 5 and 6 show the integrated TEXES spectra in the northern and southern hemispheres, respectively. From the comparison with synthetic spectra, we infer a mean H_2O_2 vmr of 45 ± 10 ppbv (2σ error bars) in the northern hemisphere, and a 2σ upper limit of 10 ppbv in the southern hemisphere, in good agreement with the climate model predictions (Fig. 4).

3. Ls = 209° (July 2018)

Our observing run took place between July 6 and July 14, 2018 (Ls = 206–211°). At that time, the planet was surrounded by a strong global dust storm that affected the temperature profile and the dust content significantly. The Martian diameter ranged from 21.9 to 23.2 arcsec, with an illumination factor above 97.7%. Two spectral intervals were recorded, at 1232–1238 and at 1237–1242 cm^{-1}. The mean Doppler shift was +0.024 cm^{-1}. Data were recorded in the same way as described above for the May 2016 observations. The observing time for a full map was about one hour. The observations are summarized in Table 1.

Table 1. Summary of TEXES observations of Mars in July 2018.

Date of obs.	Time (UT)	SEP W long.	SSP W long.	Frequency range (cm^{-1})
2018/07/06	14:02:31	101.0	118.7	1232–1238
2018/07/10	13:30:57	57.8	72.7	1232–1238
2018/07/11	10:27:22	5.0	19.2	1237–1242
2018/07/11	13:21:45	46.4	60.6	1232–1238
2018/07/14	10:25:16	338.1	350.2	1232–1238

3.1. The 1234 cm^{-1} region

Figure 7 shows the four spectra recorded in July 2018 in the 1233.6–1234.5 cm^{-1} spectral range. A comparison with Fig. 1 shows that the CO_2 line depths are weaker than in our May 2016 observation. This is the effect of the global dust storm, which decreases the atmospheric temperature gradient and the temperature contrast between the atmosphere and the surface. It can be seen that the H_2O_2 doublet, easily identified in the northern hemisphere in our May 2016 observation, is undetected.

We first selected the disk-integrated spectrum of July 11, 2018. To model the H_2O_2 spectrum, we used a temperature profile extracted from the MCD for a high dust content. This profile assumes a temperature of 248 K at an altitude of 1 km, an isothermal profile at 245 K between 1 and 20 km, and a temperature of 200 K at 50 km. The surface pressure was 5 mbar,

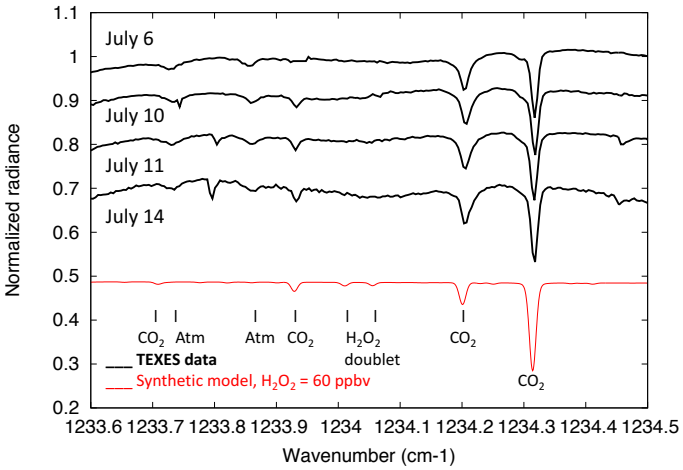

Fig. 7. Black lines: normalized disk-integrated spectra of Mars between 1233.6 and 1234.5 cm^{-1}, recorded on July 6, 10, 11, and 14, 2018, shifted vertically by 0.0, −0.1, −0.2, and −0.3, respectively. In the July 6 spectrum, a spike was present at 1233.93 cm^{-1}, at the position of the CO_2 line, and has been removed. Red line: synthetic model, calculated using the atmospheric parameters described in Sect. 3.1, with $H_2O_2 = 60$ ppbv, shifted by −0.5. The spectral resolution of the models is 0.014 cm^{-1}.

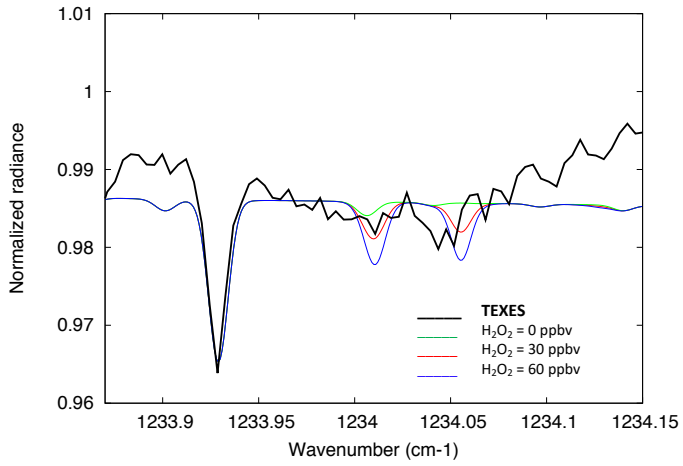

Fig. 8. Black line: normalized disk-integrated spectra of Mars between 1233.60 and 1234.50 cm^{-1}, recorded on July 11, 2018. Colored lines indicate the synthetic models, calculated using the atmospheric parameters described in Sect. 3.1: $H_2O_2 = 0$ ppbv (green), 30 ppbv (red), and 60 ppbv (blue). H_2O_2 is undetected. The spectral resolution of the models is 0.014 cm^{-1}.

and we adjusted the surface temperature at 251 K in order to fit the CO_2 transition at 1233.929 cm^{-1}. During southern spring, Fig. 8 shows a comparison of our spectrum with synthetic models, calculated for different values of the H_2O_2 vmr, assuming a constant mixing ratio. It can be seen that the noise level of the TEXES spectrum does not allow us to derive a significant upper limit.

In order to improve our H_2O_2 upper limit, we co-added the four spectra recorded around 1234 cm^{-1} in July 2018. Because of the presence of an artifact near the CO_2 line on July 6 (also present in 2016, as mentioned above), we removed the July 6 spectrum for the summation below 1233.95 cm^{-1}, and we kept the four spectra above this frequency. Figure 9 shows the resulting spectrum, corrected for the slope variations shown in Figs. 7 and 8. To do so, we used two straight lines of different slopes, below and above 1234.05 cm^{-1}, in order to remove the slope difference in the continuum (see Fig. 8). We estimate the 3σ

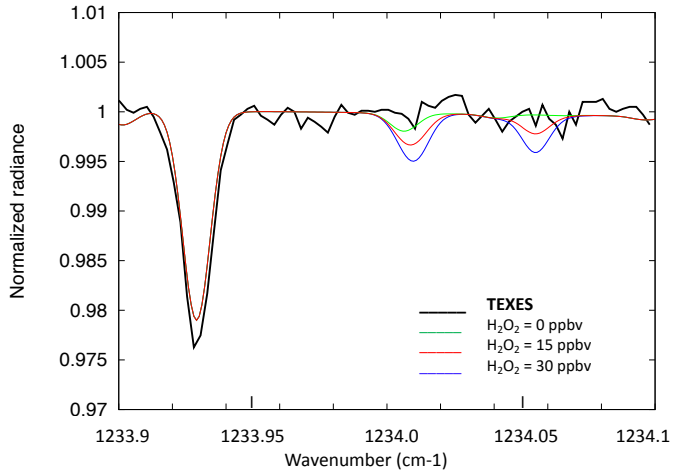

Fig. 9. Black line: averaged disk-integrated spectra of Mars between 1233.90 and 1234.10 cm^{-1}, obtained from the summation of the four spectra shown in Fig. 7. For the July 6 spectrum, a spike appeared at the position of the CO_2 line at 1233.93 cm^{-1}, so the averaged CO_2 line was obtained from the summation of the three other spectra. Synthetic models were calculated using the atmospheric parameters described in Sect. 3.1, with $H_2O_2 = 0$ ppbv (green line), 15 ppbv (red line), and 30 ppbv (blue line). H_2O_2 is undetected, with a 2σ upper limit of 15 ppbv. The spectral resolution of the models is 0.014 cm^{-1}.

peak-to-peak fluctuations of the spectrum to be 0.003. Comparison with the models shows that a H_2O_2 volume mixing ratio of 15 ppbv corresponds to a line depth of 0.002. We thus derive from the 1234 cm^{-1} data a 2σ upper limit of 15 ppbv.

We wondered whether the H_2O_2 distribution over the disk might be very inhomogeneous, as observed in May 2016. For this reason, we mapped the line depths of CO_2 and H_2O_2 as we did for our previous observations. Figure 10 shows, as an example, the maps of the continuum radiance at 1233.98 cm^{-1}, the CO_2 line depth at 1233.93 cm^{-1}, and the line depth of the H_2O_2 line at 1234.05 cm^{-1} corresponding to the map of July 11, 2018. The H_2O_2 line depth map shows that the H_2O_2 abundance is close to zero everywhere on the Martian disk.

For comparison, Fig. 11 shows the synthetics maps of the surface temperature and the temperature contrast $T(z = 1\text{km}) - T_S$ for two different scenarios, the normal case and the dusty case (MY 25), derived from the LMD-MGCM under the same observing conditions. The continuum radiance observed in July 2018 (Fig. 10) exhibits lower values than in Fig. 2, with a maximum that is two times lower. This is due to the lower daytime surface temperature, and to a stronger contribution from the dust-laden atmosphere. The CO_2 line depth is very different from that in Fig. 2, which probably reflects a different distribution of the dust at this period. During the global dust storm, the dust opacity was high at every longitude and latitude, except north of about 40° N (Kass et al. 2018). It is thus likely that our planetary averaged spectra are mostly sensitive to the less dusty middle and high northern latitudes.

3.2. The 1241 cm^{-1} region

In the 1241 cm^{-1} spectral range, a single map was obtained on July 11, 2018. As in many previous measurements, we used the H_2O_2 doublet around 1241 cm^{-1}, but this time with the GEISA 2015 database. The H_2O_2 doublet appears at 1241.533 cm^{-1} ($I = 3.60 \times 10^{-20}$ cm molec^{-1}, $E = 155.502$ cm^{-1}, and at 1241.613 cm^{-1} ($I = 3.37 \times 10^{-20}$ cm molec^{-1}, $E = 163.185$ cm^{-1}). It brackets a weak (unresolved) CO_2 doublet (1241.574 and 1241.580 cm^{-1},

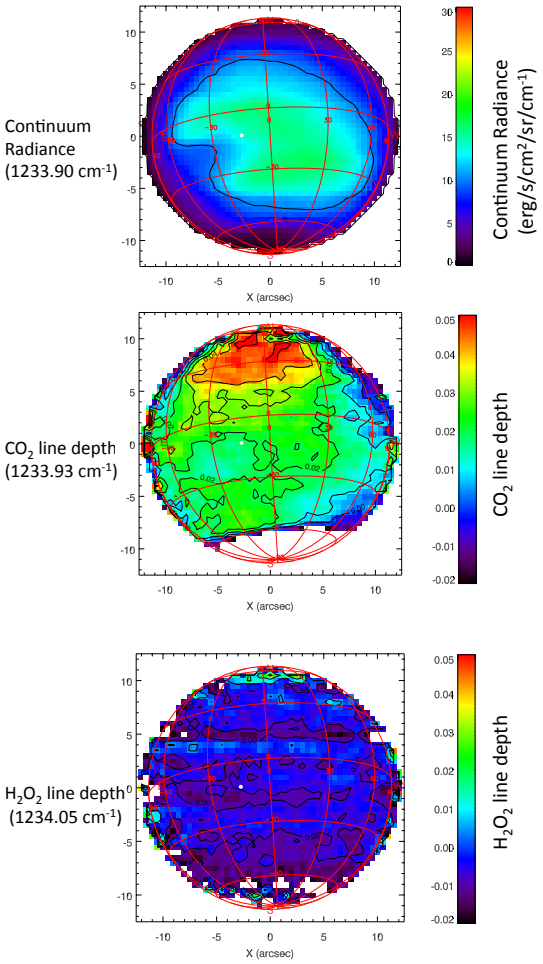

Fig. 10. Maps of the continuum radiance at 1233.90 cm^{-1} (*top*), the CO_2 line depth at 1233.93 cm^{-1} (*middle*), and the H_2O_2 line depth at 1234.05 cm^{-1} (*bottom*), corresponding to the 1234 cm^{-1} map of July 11, 2018. H_2O_2 is undetected. The Martian north pole is at the top of the figure. The subsolar point is shown as a white dot.

$I = 5.15 \times 10^{-27}$ cm molec^{-1}, $E = 664.59$ cm^{-1}). As mentioned above, the intensities of the H_2O_2 lines are higher than the GEISA 2003 values by a factor of about 1.75. The implications of this change are discussed in Sect. 4.

Figure 12 shows the disk-integrated spectrum of Mars corresponding to this map, in the 1241.5–1241.65 cm^{-1} spectral range. As in the previous case, there is no clear detection of the H_2O_2 doublet. The strong fluctuations of the continuum in the immediate vicinity of the H_2O_2 doublet, and the short spectral interval available for measuring it, make the comparison with synthetic models more difficult than in the previous case. We tentatively estimate the 3σ peak-to-peak continuum fluctuations to be 0.004. A H_2O_2 volume mixing ratio of 10 ppbv corresponds to a depth of 0.002. We thus derive a 2σ upper limit of 15 ppbv for the mean H_2O_2 vmr over the Martian disk.

As in the case of the 1234 cm^{-1} data, we mapped the line depths of CO_2 and H_2O_2 to search for possible variations in the H_2O_2 abundance over the disk. Figure 13 shows the maps of the continuum radiance at 1241.60 cm^{-1}, the CO_2 line depth at 1241.62 cm^{-1}, and the line depth of the H_2O_2 line at 1241.57 cm^{-1}. As in the previous case, there is no evidence of any enhancement of the H_2O_2 abundance over the Martian disk.

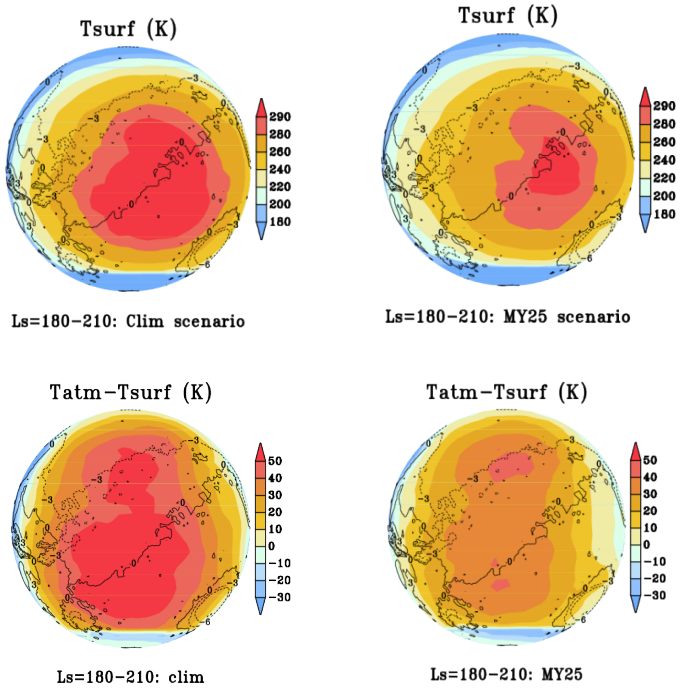

Fig. 11. Synthetic maps of (*top*) the surface temperature, and (*bottom*) the temperature contrast $T(z = 1\text{km}) - Ts$, assuming the standard scenario (*left*) and the MY 25 dust scenario. The seasonal range is Ls = 180–210°. The maps are extracted from the Mars Climate Database (Forget et al. 1999).

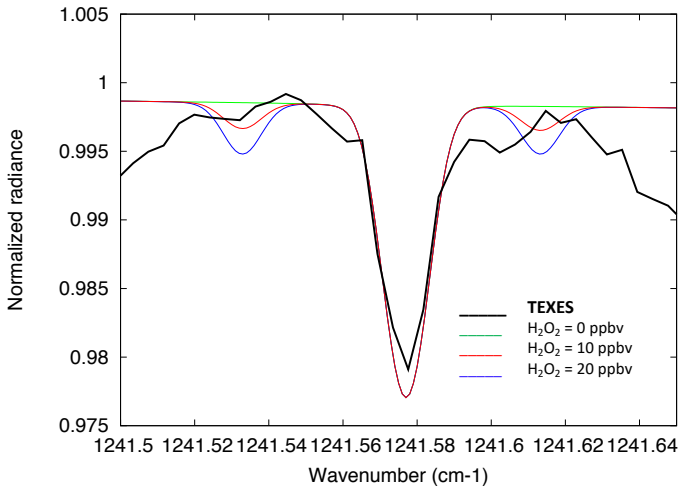

Fig. 12. Black line: normalized disk-integrated spectra of Mars between 1241.50 and 1241.65 cm^{-1}, recorded on July 11, 2018. The synthetic models are calculated using the atmospheric parameters described in Sect. 3.1: Green: $H_2O_2 = 0$ ppbv; red: $H_2O_2 = 10$ ppbv; blue: $H_2O_2 = 20$ ppbv. H_2O_2 is undetected, with a 2σ upper limit of 15 ppbv. The spectral resolution of the models is 0.014 cm^{-1}.

3.3. Validity of the radiative transfer code in the case of dusty conditions

In all our previous analyses, we used a line-by-line radiative transfer without scattering, which was found to be reliable for calculating the thermal infrared spectrum of Mars under normal dust conditions. In the case of our July 2018 observations, we needed to check the validity of our code in the conditions of a global dust storm. We used a radiative transfer code

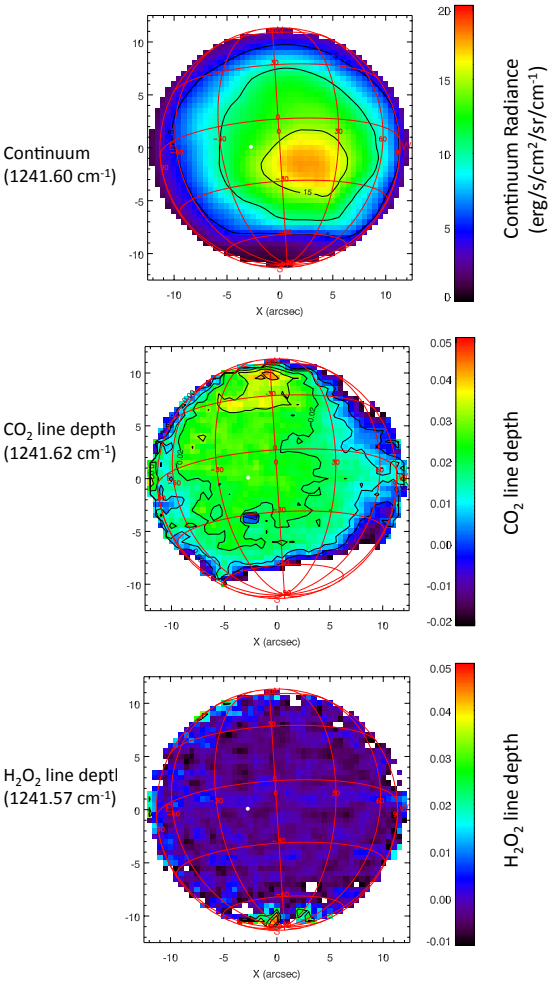

Fig. 13. Maps of the continuum radiance at 1241.60 cm^{-1} (*top*), the CO_2 line depth at 1241.62 cm^{-1} (*middle*), and the H_2O_2 line depth at 1241.57 cm^{-1} (*bottom*), corresponding to the 1241 observation of July 11, 2018. H_2O_2 is undetected. The Martian north pole is at the top of the figure. The subsolar point is shown (white dot).

including multiple scattering (Aoki et al. 2018) and we modeled the 1241.52–1241.63 cm^{-1} spectral range, including the H_2O_2 doublet and the CO_2 line found in this range, assuming a global dust scenario similar to MY 25 (Daerden et al. 2019). We have assumed H_2O_2 and CO_2 to be uniformly mixed. Results are shown in Fig. 14. In this model the dust opacity is equal to 3.5–4 in the latitude range (30N–60S), corresponding to the geometry of our observations.

It can be seen that taking into account multiple scattering has an effect on the H_2O_2/CO_2 line depth ratio. For a H_2O_2 vmr of 10 ppbv, the ratio derived using the 1241.533 cm^{-1} H_2O_2 transition is equal to 0.10 using the radiative transfer code without multiple scattering (Fig. 12) and to 0.17 using the multiple scattering code (Fig. 14). As a result, the H_2O_2 2σ upper limit derived from this calculation is 10 ppbv, even lower than in the previous case. This illustrates that the simple line depth ratio method tends to overestimate the H_2O_2 vmr if it is used in the case of a global dust storm. We also note that, because some quantity of dust is present everywhere on Mars at any season, all TEXES measurements of H_2O_2 retrieved using the line depth ratio method could be slightly lowered by this effect; in particular, the upper limit derived for the 2001 measurement is expected to be further lowered.

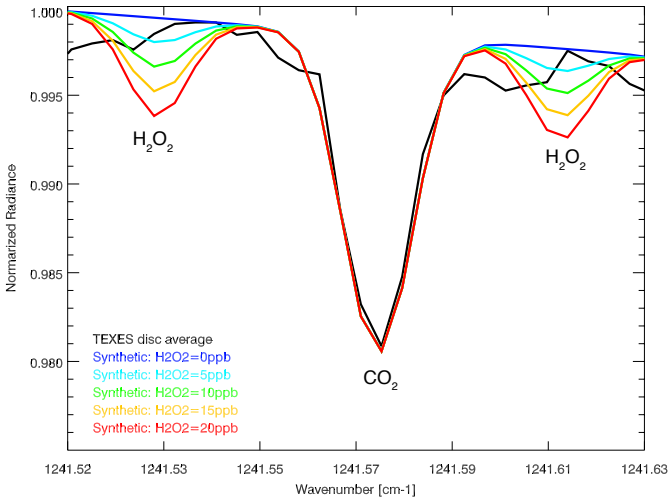

Fig. 14. Black curve: normalized disk-integrated spectrum of Mars between 1241.52 and 1241.63 cm^{-1}, recorded by TEXES on July 11, 2018 (as in Fig. 12). Colored lines indicate the synthetic spectra calculated with multiple scattering under the conditions of a global dust storm (see Sect. 3.3) for various values of the H_2O_2 vmr: 20 ppbv (red), 15 ppbv (orange), 10 ppbv (green), 5 ppbv (light blue), and 0 ppbv (blue). H_2O_2 is undetected in the TEXES spectrum, with a 2σ upper limit of 10 ppbv.

4. Discussion

4.1. Recalibration of the H_2O_2 dataset

In order to analyze the seasonal variations in H_2O_2 and to compare them with global climate models, we first needed to recalibrate the previous TEXES measurements using the GEISA-2015 database.

For all TEXES observations of H_2O_2 between 2001 and 2014, we had been using the GEISA 2003 database. Its content is described in Jacquinet-Husson et al. (1999, 2005, 2008). The H_2O_2 spectroscopic parameters were updated from the previous GEISA version using the work of Flaud et al. (1989), Camy-Peyret et al. (1992), and Perrin et al. (1996), where a detailed description of the linelist can be found. A significant update of this list occurred in the 2011 edition of the GEISA database, described in Jacquinet-Husson et al. (2011). The parameters of the ν_6 band of H_2O_2, centered at 7.9 μm, were completely replaced, leading to improved line positions and intensities, due to the inclusion of several torsional-vibration sub-bands. The line intensities are more accurate as these parameters are based on new line intensity measurements and on a sophisticated theoretical treatment that accounts for the torsional effect (Perrin et al. 1995; Klee et al. 1999). Concerning our H_2O_2 analysis with TEXES, the change from GEISA 2003 to GEISA 2015 translates into a significant increase in the intensities of the H_2O_2 transitions. In the case of the 1234 cm^{-1} doublet, the intensities are stronger by a factor of 1.74 at 1234.011 cm^{-1} and 1.80 at 1234.055 cm^{-1}. The two components of the H_2O_2 doublet around 1241 cm^{-1} are stronger by a factor of 1.78 at 1241.53 cm^{-1} and 1.74 at 1241.61 cm^{-1}. Since we used an average of the two components of the 1241 cm^{-1} doublet in our previous analyses, we corrected the previous results obtained with this doublet by dividing our earlier H_2O_2 measurements by a factor of 1.76. We also note a slight change (0.01 cm^{-1}) in the position of the 1234.011 cm^{-1} line (previously assigned at 1234.002 cm^{-1}), which provides a better agreement with the TEXES data of June 2003 (Encrenaz et al. 2004). Finally, we

Table 2. Summary of H_2O_2 measurements between 2001 and 2018.

Ls	Date of obs.	MY	Observation	H_2O_2 vmr GEISA 2003 (ppbv)	H_2O_2 vmr GEISA 2015 (ppbv)	H_2O_2 vmr submm (ppbv)	H_2O column density pr-μm
77	2010, April 16	30	*Herschel*/HIFI			3 (u.l.)	15 [(1)]
80	2008, May 30–June 3	28	TEXES	10 ± 5	5.7 ± 2.9		10 [(1)], 15 [(2)]
96	2014, March 1	32	TEXES	15 ± 7	8.6 ± 4.0		27 [(2)]
112	2001, Feb 1–3	25	TEXES	10 (u.l.)	6 (u.l.)		25 [(3)]
148	2016, May 16	33	TEXES		45 ± 10		16.5 [(4)]
156	2014, July 2–4	32	TEXES	30 ± 7	17.0 ± 4.0		22 [(2)]
206	2003, June 19–20	26	TEXES	32 ± 7	18.2 ± 4.0		18 [(2)]
209	2018, July 6–14	34	TEXES		10 (u.l.)		14.5 [(4)]
250	2003, Sept 4	26	JCMT			18.0 ± 4.0	
332	2005, Nov 30–Dec 1	27	TEXES	15 ± 10	8.6 ± 5.7		10 [(1)], 9 [(2)]
352	2009, Oct 11–15	29	TEXES	15 ± 10	8.6 ± 5.7		10 [(1)], 6 [(2)]

Notes. The water content corresponding to these measurements is shown in the last column. Origin: [(1)]SPICAM (Montmessin et al. 2017), [(2)]TEXES, [(3)]TES (Smith 2004), and [(4)]PFS/Mars Express (Giuranna, priv. comm.). u.l.: 2σ upper limit.

note that the spectroscopic parameters of the ν_6 band of H_2O_2, listed in GEISA-2015 and used in the present study, are identical to those of the HITRAN 2016 database.

Table 2 summarizes the H_2O_2 observations from 2001 until now, with the corresponding Martian year of each observation, including the H_2O_2 values corresponding to the previous GEISA 2003 and the updated GEISA 2015 values. For each H_2O_2 measurement, an estimate of the water vapor content is indicated for the same time and the same latitude. Data for H_2O were taken from the TEXES observations when they were available, and from the TES instrument aboard the Mars Global Surveyor (Smith 2004) and SPICAM aboard Mars Express (Montmessin et al. 2017) in the other cases. In the case of the TEXES measurements, the water vapor mixing ratios were converted to column densities: for a surface pressure of 6.5 mbars, a H_2O vmr of 250 ppm corresponds to a column density of 15 pr-μm (Encrenaz et al. 2010). Table 2 shows that, in many cases, a high content of H_2O_2 is associated with a large water content. This is not surprising, as H_2O_2 is formed from the recombination of two HO_2 radicals resulting from the H_2O photodissociation (see, e.g., Clancy & Nair 1996; Krasnopolsky 2006, 2009). The relationship between the H_2O and H_2O_2 abundances is discussed in more detail below (Sect. 4.2). The comparison of the observed seasonal variations in H_2O_2 with the models is analyzed in Sect. 4.3.

Figure 15 summarizes all measurements of H_2O_2 on Mars as a function of the seasonal cycle. Because these measurements were all performed from Earth (or from near the Earth in the case of *Herschel*), the data of northern spring and summer (Ls = 0–180°) refer to the northern hemisphere, while the data of southern spring and summer refer to the southern hemisphere. It can be seen that the measured H_2O_2 values are now globally below the predictions. In addition, there are four values of Ls (around 70°, 100°, 150°, and 200°) for which H_2O_2 observations show contradictory results between two different Martian years. We discuss below the case of the last one, which corresponds to our last observation performed in July 2018.

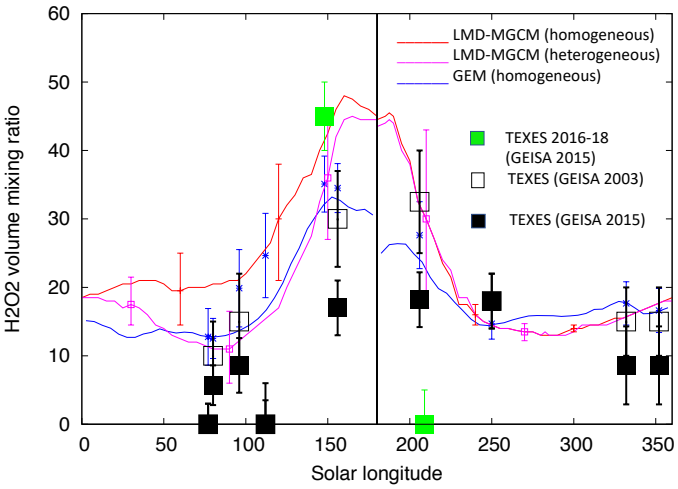

Fig. 15. Seasonal cycle of H_2O_2 on Mars integrated over the Martian disk. The ordinate is the H_2O_2 volume mixing ratio in ppbv. Observed regions are centered over 20° N during northern spring and summer, and around 20° S during northern autumn and winter. Open squares: previous TEXES measurements of H_2O_2 (using GEISA 2003). Green squares: new TEXES observations (this paper). Black squares: recalibrated TEXES measurements of H_2O_2 (using GEISA 2015) and submillimeter measurements. Red curve: 3D global climate (LMD-MGCM) model including gas phase chemistry; purple curve: LMD-MGCM model considering heterogeneous chemistry on water ice grains (Lefèvre et al. 2008). The error bars correspond to the 1σ standard deviation of the H_2O_2 mean volume mixing ratio along the ±20° latitude parallel. Blue curve: 3D GEM model including gas phase chemistry (Daerden et al. 2019). All curves are calculated for a latitude of 20° N for Ls = 0–180° and 20° S for Ls = 180–360°, in order to account for the observing conditions. Blue crosses: H_2O_2 abundances inferred from the GEM model (Daerden et al. 2019) corresponding to the exact geometry of the observations. The black vertical bar indicates the autumn equinox. Error bars of the data points are $\pm\sigma$.

4.2. The H_2O_2 abundance during the MY 34 global dust storm

A strong discrepancy between the observations and the models is shown with our measurement of July 2018 (Ls = 209°, MY 34). Our H_2O_2 upper limit is in clear disagreement with all models, and also with our first detection of H_2O_2 with TEXES in June 2003 (Ls = 206°, MY 26).

A possible explanation could be the exceptional conditions of the global dust storm which took place in July 2018 and could have affected the photochemistry of H_2O_2. Space

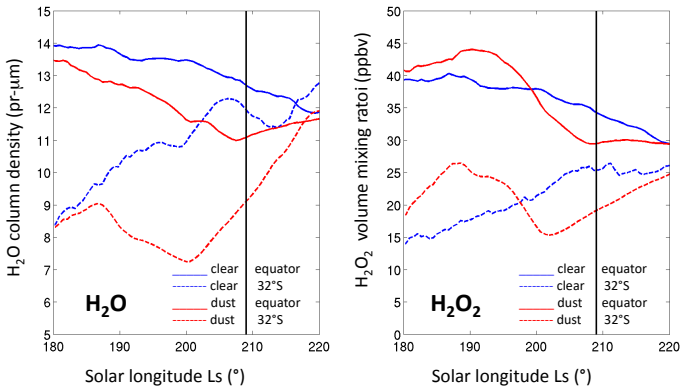

Fig. 16. Seasonal variations in the H_2O longitude-integrated column density (*left*) and the H_2O_2 longitude-integrated volume mixing ratio (*right*) during the beginning of southern summer (Ls = 180°–220°) in the case of a clear atmosphere (blue) and during a global dust storm (red). Solid curves: equator; dashed curves: 32S longitude. The black vertical line indicates the solar longitude corresponding to the TEXES observation.

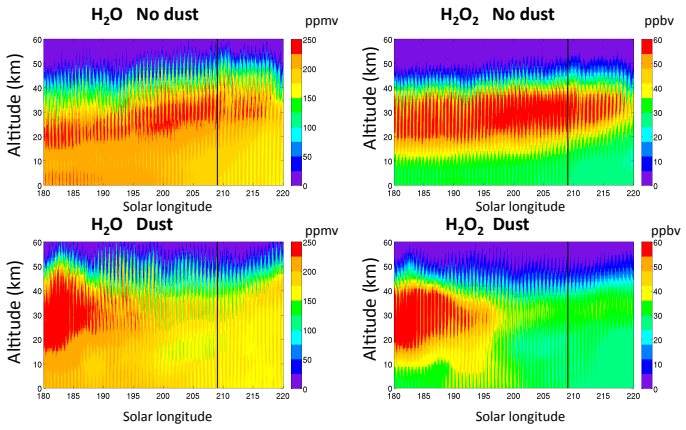

Fig. 17. Vertical distributions of H_2O (*left*) and H_2O_2 (*right*) as a function of the solar longitude at the beginning of southern summer (Ls = 180–220°) *Top*: clear conditions; *bottom*: dusty conditions. Simulations were done with the GEM model (Daerden et al. 2019) for the latitude of the subsolar point (12° S).

observations from orbit during the previous global dust storm in 2007 showed a decrease in the total water column at low latitudes (Trokhimovskiy et al. 2015; Smith et al. 2018). In addition, vertical sampling of water vapor by SPICAM on Mars Express showed a strong increase in water vapor at high altitudes and latitudes (Fedorova et al. 2018); this finding was confirmed by more sensitive and detailed observations from TGO during the 2018 global dust storm (Vandaele et al. 2019). A possible interpretation is that during a global dust storm, as the strongly increased dust abundances in the atmosphere cause more heating by absorption of solar light, they cause an enhanced global circulation and thus more transport of air (including water vapor) from the equatorial region to the higher latitudes. Water vapor is redistributed from lower to higher latitudes, leading to a decrease in the water column at low latitudes. As mentioned above, H_2O_2 results from a nocturnal recombination of two HO_2 molecules, which are the primary photolysis products of water vapor. Recent photochemical models (Daerden et al. 2019) indeed confirm a correlation between the columns of H_2O and H_2O_2, already pointed out previously (e.g., Clancy & Nair 1996; Krasnopolsky 2009). An example of this effect is shown in Fig. 16, which shows that a decrease in H_2O by about 25% is expected in the southern hemisphere during a global dust storm, translating into a depletion of H_2O_2 by about the same factor in the same latitude range. In addition, in Fig. 17, a GEM simulation (Daerden et al. 2019) shows the expected behavior of the H_2O and H_2O_2 vertical distributions during the beginning of southern summer, in the case of a clear atmosphere and under dusty conditions, at the latitude of the subsolar point at the time of the July 2018 observations (12° S). For Ls = 209°, both molecules are depleted, especially at high altitude, resulting in a depletion of their column densities.

The decrease in water vapor during the 2018 global dust storm was measured by the Planetary Fourier Spectrometer (PFS) instrument aboard Mars Express (Giuranna & Wolkenberg 2019). Figure 18 shows the latitudinal profile of H_2O at the time of the TEXES observations (MY 34, Ls = 205–215°), as derived from PFS observations. It can be seen that the H_2O column density is depleted by a factor of almost 2 with respect to MY 29, a Martian year corresponding to a low dust content. This seems to imply that the dust content during the MY 34 global dust storm

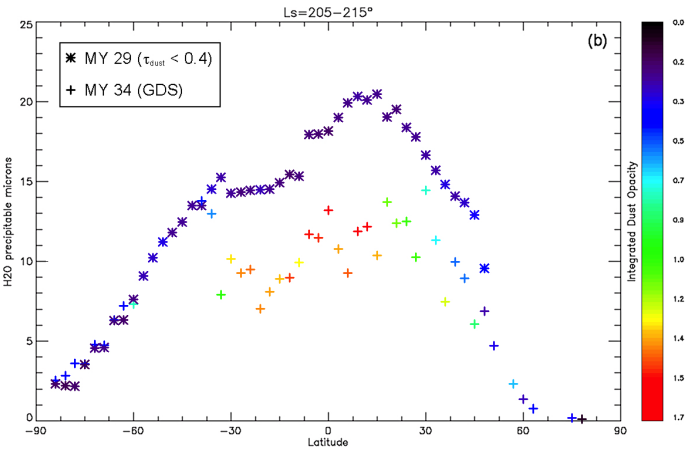

Fig. 18. Latitudinal variations in the water vapor column density observed by PFS berween Ls = 205° and 215° in the case of MY 29, corresponding to a dust opacity lower than 0.4 (stars), and M34, a great dust storm (crosses). The color bar on the right of the figure indicates the integrated dust opacity. The figure is taken from Giuranna & Wolkenberg (2019).

was actually higher than assumed in the simulations shown in Figs. 14 and 15. A factor 2 decrease of H_2O column density might have led to a similar depletion of the H_2O_2 column density. The decrease of water vapor at middle latitudes is thus a plausible explanation for the low upper limit of H_2O_2 inferred by TEXES.

The depletion of water vapor in the Martian atmosphere in the presence of a high dust content is being studied in detail by Giuranna & Wolkenberg (2019). This paper, based on the PFS database, shows that H_2O was strongly depleted during the MY 28 and MY 34 global dust storms. As a possible explanation, the authors suggest that the water vapor depletion could be due to the shading of the surface by the optically thick dust and the subsequent cooling of the surface, which would lead to water adsorption by the regolith, acting as a relative sink for water during the course of the dust storm (Boettger et al. 2004, 2005). Another possible explanation, proposed by Fouchet et al. (2011), is the nearly isothermal profile that would prevent convection from the boundary layer to the general convection cell.

4.3. Seasonal behavior of H_2O_2

As shown in Fig. 15, the recalibration of the H_2O_2 dataset has an important impact on our understanding of the seasonal behavior of H_2O_2. First, the general overall agreement mentioned in earlier publications is significantly degraded. Second, we can see on four occasions (Ls = 77, 112, 150, and 209°) that there is a contradiction between the H_2O_2 measurements recorded at the same season during different Martian years. We showed that the presence of the MY 34 global dust storm can explain the low value of H_2O_2 in July 2018 (Ls = 109°). However, three other cases remain unexplained. Two of them occur near aphelion, and the third occurs before the autumn equinox. The good agreement observed between the H_2O_2 observation of May 2016 (Ls = 148.5°) and the models could indicate that, while the normal seasonal behavior of H_2O_2 is accurately described by the models, another factor of unknown origin occasionally inhibits the H_2O_2 production.

A final remark has to be made about the need to use heterogeneous chemistry to account for the seasonal variations in H_2O_2. It was pointed out in our previous studies that the H_2O_2 measurements tended to support the heterogeneous model developed by Lefèvre et al. (2008). However, Fig. 15 shows that the recent GEM model developed by Daerden et al. (2019), which does not include heterogeneous chemistry, is close to the heterogeneous model of Lefèvre et al. (2008) in the seasons for which data are available; it is also closer to the data than the LMD-MGCM model for Ls around 150° and 200°. Further investigations are ongoing to better understand the differences between the two models. Our new measurement of May 2016, if we take into account the error bars, is in agreement with the two models; however, it does not help us to discriminate between the gas phase and the heterogeneous photochemical models, as the two models are consistent within the error bars at that time of the season.

5. Conclusions

In this paper, we described two observations of H_2O_2 on Mars obtained near the 2016 and 2018 oppositions, when the diameter of Mars was 17 and 23 arcsec, respectively. The May 2016 observation was obtained near the southern equinox (Ls = 148.5°), when the H_2O_2 abundance is expected to be at its maximum. Our result (45 ± 10 ppbv in the northern hemisphere) is in agreement with the LMD-MGCM models of Lefèvre et al. (2008) and also, more marginally, with the GEM model of Daerden et al. (2019). Our second observation (July 2018, Ls = 209°) took place in the middle of the M34 global dust storm. In contrast with our first observation of June 2003 (Ls = 206°, $H_2O_2 = 18.2 \pm 4.0$ ppbv), we obtained a stringent 2σ upper limit of 10 ppbv. Based on PFS observations of the water vapor content at the same time (Giuranna & Wolkenberg 2019), and GEM simulations by Daerden et al. (2019), we propose that the H_2O_2 depletion is due to the depletion of water, which leads to the lack of HO_2 radicals.

Comparison between the recalibrated H_2O_2 dataset and the different models suggests that overall the observed abundance of H_2O_2 is lower than predicted, in turn suggesting that the Martian atmosphere is less oxydizing than expected by photochemical models. It should also be noted that the GEM model using gas-phase chemistry (Daerden et al. 2019) and the LMD-MGCM model using heterogeneous chemistry (Lefèvre et al. 2008) are generally consistent, and both are above the observed seasonal variations in H_2O_2. As a consequence, our earlier conclusion about the indication of heterogeneous chemistry in the photochemical cycle of H_2O_2 may have to be revisited. Finally, the evidence for inter-annual variabilities of H_2O_2 requires further investigations using photochemical models. In the future, measurements should concentrate on the season around the autumn equinox (Ls = 150–230°), when the difference between the two models is greatest.

Acknowledgements. T.E. and T.K.G. were visiting astronomers at the Infrared Telescope Facility, which is operated by the University of Hawaii under cooperative agreement no. NNX-08AE38A with the national Aeronautics and Space Administration, Science Mission Doctorate, Planetary Astronomy Program. We wish to thank the IRTF staff for the support of the TEXES observations. T.K.G. acknowledges the support of NASA Grant NNX14AG34G. T.E. and B.B. acknowledge support from CNRS and the Programme National de Planétologie.

References

Aoki, S., Richter, M., DeWitt, C., et al. 2018, A&A, 610, A78
Atreya, S. K., & Gu, Z. G. 1995, Adv. Space Res., 16, 57
Boettger, H. M., Lewis, S. R., Read, P. L., & Forget, F. 2004, Geophys. Res. Lett., 31, L22702
Boettger, H. M., Lewis, S. R., Read, P. L., & Forget, F. 2005, Icarus, 177, 174
Camy-Peyret, C., Flaud, J.-M., Johns, J. W. C., & Noel, M. 1992, J. Mol. Spectr., 155, 84
Clancy, R. T., & Nair, H. 1996, J. Geophys. Res., 101, 12785
Clancy, R. T., Sandor, B. J., & Moriarty-Schieven, G. H. 2004, Icarus, 168, 116
Daerden, F., Neary, L., Viscardy, S., et al. 2019, Icarus, 326, 197
Encrenaz, T., Bézard, B., Greathouse, T. K., et al. 2004, Icarus, 170, 424
Encrenaz, T., Greathouse, T., Bézard, B., et al. 2010, A&A, 520, A33
Encrenaz, T., Greathouse, T. K., Lefèvre, F., et al. 2012, Planet. Space Sci., 68, 3
Encrenaz, T., Greathouse, T., Lefèvre, F., et al. 2015, A&A, 528, A127
Fedorova, A., Bertaux, J.-L., Betsis, D., et al. 2018, Icarus, 300, 440
Flaud, J.-M., Camy-Peyret, C., John, J. W. C., & Carli, B. 1989, J. Chem. Phys., 91, 1504
Forget, F., Hourdin, F., Fournier, R., et al. 1999, J. Geophys. Res., 104, 24155
Fouchet, T., Moreno, R., Lellouch, E., et al. 2011, Planet. Space Sci., 59, 683
Giuranna, M., & Wolkenberg, P. 2019, Icarus, submitted
Jacquinet-Husson, N., Arié, E., Ballard, J., et al. 1999, J. Quant. Spectr. Rad. Transf., 62, 205
Jacquinet-Husson, N., Scott, N. A., Chédin, A., et al. 2005, J. Quant. Spectr. Rad. Transf., 95, 429
Jacquinet-Husson, N., Scott, N. A., Chédin, A., et al. 2008, J. Quant. Spectr. Rad. Transf., 109, 1043
Jacquinet-Husson, N., Crepeau, L., Armante, R., et al. 2011, J. Quant. Spectr. Rad. Transf., 112, 2395
Jacquinet-Husson, N., Armante, R., Scott, N. A., et al. 2016, J. Mol. Spectr., 327, 31
Kass, D. M., Kleinboehl, A., Shirley, J. H., et al. 2018, Communication presented at the AGU Fall Meeting, 10–14 Dec. 2018, Washington DC, USA
Klee, S., Winnewisser, M., Perrin, A., & Flaud, J.-M. 1999, J. Mol. Spectr., 195, 154
Krasnopolsky, V. A. 1993, Icarus, 101, 313
Krasnopolsky, V. A. 2006, Icarus, 185, 157
Krasnopolsky, V. A. 2009, Icarus, 201, 564
Lacy, J. H., Richter, M. J., Greathouse, T. K., et al. 2002, PASP, 114, 153
Lefèvre, F., Bertaux, J.-L., Clancy, R. T., et al. 2008, Nature, 454, 971
Montmessin, F., Korablev, O., Lefèvre, F., et al. 2017, Icarus, 297, 195
Moudden, Y. 2007, Planet. Space Sci., 55, 2137
Oyama, V. I., & Berdahl, B. J. 1977, J. Geophys. Res., 82, 4669
Perrin, A., Valentin, L., Flaud, J.-M., et al. 1995, J. Mol. Spectr., 171, 358
Perrin, A., Flaud, J.-M., Camy-Peyret, C., et al. 1996, J. Mol. Spectr., 176, 287
Pollack, J. B., Dalton, J. B., Grinspoon, D., et al. 1993, Icarus, 103, 1
Smith, M. D. 2004, Icarus, 167, 148
Smith, M., Daerden, F., Neary, L., & Khayat, A. 2018, Icarus, 301, 117
Trokhimovskiy, A., Fedorova, A., Korablev, O., et al. 2015, Icarus, 251, 50
Vandaele, A. C., Betsis D., Ivanov Y. S., et al. 2019, Nature, 568, 521